Composite Functional Materials

2025, 1(2): 20250204 https://doi.org/10.63823/20250204

RESEARCH ARTICLE

Bronze TiO_2 photocatalysis facilitates solution plasma production of H_2O_2

Yanhui Li, Changhua Wang*, Qi Wu, Yuanyuan Li, Shuang Liang, Dexin Jin, He Ma, Xintong Zhang*

State Key Laboratory of Integrated Optoelectronics, Key Laboratory of UV-Emitting Materials and Technology of Chinese Ministry of Education, Department of Physics, Northeast Normal University, 5268 Renmin Street, Changchun 130024, China

ABSTRACT: Synergizing photocatalysis with external fields offers a promising strategy to surpass limitations of single catalytic systems, yet designing catalysts that works in multi-field remains challenging. In this work, we explore catalysts that improves photocatalysis in solution plasma to significantly enhance H_2O_2 production. We focus on bronze TiO_2 and tune its crystallinity through an adjusted sodium titanate precursor route. In particular, the regular and wide tunnel structure of $Na_2Ti_6O_{13}$ precursor results in bronze TiO_2 with exceptional crystallinity. Upon introducing highly crystalline bronze TiO_2 nanobelts into solution plasma, we effectively suppress the photocatalytic decomposition of H_2O_2 in plasma field, reducing the decomposition rate by 70% compared to commercial P25 TiO_2 photocatalysts. Further carbon coating results in H_2O_2 concentrations up to 3.7 mmol/L, which is 1-3 orders of magnitude higher than most photocatalytic systems. Our work elucidates the potential photocatalytic effects within solution plasma and achieves synergy between photocatalysis and solution plasma.

KEYWORDS: Solution Plasma, photocatalysis, Bronze TiO_2, H_2O_2 production

1. Introduction

Photocatalysis is widely adopted but faces challenges like low reaction rates, poor selectivity, and low efficiency [1]. A promising approach to address these limitations is the integration of photocatalysis with external fields. For instance, combining photocatalysis with thermal energy can accelerate molecular diffusion and improve product selectivity via electron-phonon coupling [2-4]. Coupling photocatalysis with an electric field can activate catalysts that are otherwise inactive [5]. Additionally, integrating photocatalysis with piezoelectric effects can achieve effective charge carrier dynamics control through the synergy of piezoelectric and semiconductor photoexcitation properties [6]. Overall, combining photocatalysis with external fields can overcome the limitations of single catalysis. Up until now, there are two types of photocatalysis coupled multi-field catalysis: one driven by external light sources [7], and the other driven by physical fields themselves, such as sonoluminescence [8], electroluminescence [9], and plasma luminescence [10]. The former and latter is

---

Received: June 19, 2025. **Revised:** December 24, 2025. **Accepted:** December 25, 2025. **Available online:** December 23, 2025

***Corresponding author:** wangch100@nenu.edu.cn (C. Wang), xtzhang@nenu.edu.cn (X. Zhang)

referred to active photocatalysis and passive photocatalysis, respectively. The modulation of passive photocatalysis can increase the utilization of luminescence and is equally important for multi-field driven catalysis. Therefore, tuning passive photocatalysis and understanding the underlying mechanisms are crucial to maximize the synergistic advantages of multi-field catalysis.

Solution plasma has emerged as a novel catalytic technology in recent years [11-13]. The strong electric field, light emission, and shock wave effects within the plasma channel could effectively activates water, decomposing it into hydroxyl radicals, which then recombine to form H_2O_2[14-16]. As an electrically driven process, it shares the green feature of photocatalysis for H_2O_2 production [17-21]. Introducing semiconductor catalysts into the solution plasma channel can further enhance the catalytic activity. Notably, solution plasma displays luminescence across the UV to visible spectrum [22], making the passive photocatalysis an important consideration. However, the study of solution plasma catalysis is still in its infancy, and systematic studies on passive photocatalysis within solution plasma are lacking. Understanding how solution plasma and passive semiconductor photocatalysis can be integrated, and whether the design of semiconductor photocatalysts can improve passive photocatalysis for efficient H_2O_2 production in solution plasma, remains a critical research question. Addressing this will be crucial for advancing the practical applications of solution plasma driven reactions.

Photocatalysis is attracting increasing attention for H_2O_2 production [23-25]. TiO_2 is the most classic photocatalyst, and studying its photocatalytic behavior in solution plasma serves as a representative case for discussing photocatalysis in plasma field. Although TiO_2-based photocatalytic production of H_2O_2 has been widely reported [26], the decomposition of H_2O_2 on TiO_2 surfaces remains a non-negligible issue [27]. Different TiO_2 crystal phases exhibit varied behaviors concerning H_2O_2 decomposition. For instance, amorphous TiO_2 can be dissolved in H_2O_2 to form complexes [28], while anatase TiO_2 strongly adsorbs and decomposes H_2O_2[29], but to a lesser extent than amorphous TiO_2. In contrast, bronze-phase TiO_2 weakly adsorbs H_2O_2, facilitating its desorption and inhibiting its decomposition more effectively than other crystal phases. Studies have proven that the (001) facet of bronze-phase TiO_2 is particularly advantageous for weak adsorption of H_2O_2[30]. Therefore, one-dimensional bronze TiO_2 with c-axis orientation is ideal for inhibiting H_2O_2 decomposition and studying the synergistic effects in solution plasma driven production of H_2O_2.

In this work, we investigated the solution plasma-catalyzed production of H_2O_2 and explored the bronze TiO_2 photocatalyst for improved photocatalysis in solution plasma. We developed two synthesis methods for bronze-phase TiO_2 nanobelts, controlling the crystallinity of TiO_2 through $Na_2Ti_6O_{13}$ and $Na_2Ti_3O_7$ precursor routes respectively and compared them with commercial crystal phases. The differences in the performance of H_2O_2 production from TiO_2 were further analyzed through photocatalytic H_2O_2 production and decomposition experiments. The optimized bronze TiO_2 nanobelts coupled with the discharge system resulted in the highest H_2O_2 yield, increasing by 696.8 μmol/L/h compared to the system without a catalyst. The accumulated concentration reached 3.7 mmol/L within 1 hour, which is currently the champion value for TiO_2 photocatalytic systems. This developed approach opens novel avenues for the clean production of high-purity and high-concentration H_2O_2.

2. Experimental

2.1 Synthesis of bronze TiO_2

Chemicals used was described in the supporting information. Bronze TiO_2 was synthesized by proton exchange in sulfuric acid solution using sodium titanate as precursor.

Synthesis of sodium titanate: The mixture of Na_2CO_3 and P25 (the molar ratio of Na_2CO_3/TiO_2 was 1:4 and 1:2.5, respectively) was fully ground with 2 g of NaCl and 0.5 g of $Na_2HPO_4 \cdot 12H_2O$ for 20 min, and calcined in Muffle furnace at 825 °C for 8 h. The sintered samples were washed and freeze-dried. Finally, two different types of sodium titanate were obtained ($Na_2Ti_6O_{13}$ and $Na_2Ti_3O_7$, Figure S1).

Synthesis of bronze TiO_2: First, 30 mL of 0.02 M H_2SO_4 solution with 0.05 g of $Na_2Ti_6O_{13}$ powder were transferred to a 50 mL polytetrafluoroethylene reactor and heated at 170 °C for 96 h. After cooling to room temperature, the supernatant was removed, and the white sediment was washed with deionized water for several times until the solution was neutral. After filtration, the solution was freeze-dried. The obtained sample was named TiO_2(B)-1. Secondly, 500 mL of 0.02 M H_2SO_4 solution with 0.05 g of $Na_2Ti_3O_7$ powder were placed in a beaker and stirred at room temperature for 72 h. After filtering, repeat washing with deionized water for several times until the solution shows neutral. The freeze-dried sample was further annealed (450 °C, 2 h), and finally the sample was named TiO_2(B)-2.

2.2 Production of H_2O_2 by plasma-catalysis reaction system

The plasma-catalysis experimental apparatus as shown in Scheme 1, which is made up of four important parts: pulsed plasma generator, plasma-catalysis reactor, cooling circulating water and gas. The parameters of the pulsed plasma generator can be adjusted, in this study, the output pulse voltage was set as ± 3 kV, with a pulse frequency of 7 kHz and a pulse width of 3 μs. Two tungsten rods (diameter: φ = 3.0 mm, gap: 0.5 mm) are connected to both ends of the double-layer plasma reactor, which serve both as high voltage electrodes and as gas inflow channels. Prior to turning on the pulsed plasma generator, 100 ml of ultrapure water and 20 mg of catalyst were sonically dispersed in an ultrasonic pulverized for 30 min and then added to the plasma reactor. High purity gas (99.999%) was continuously added to the plasma reactor at a fixed flow rate of 1 L/min throughout the experiment. And the cooling circulating water maintains the temperature inside the reactor at 10 °C. The concentration of H_2O_2 were characterized using a UV-2600 Shimadzu UV spectrophotometer, refer to the support information for detailed testing procedures.

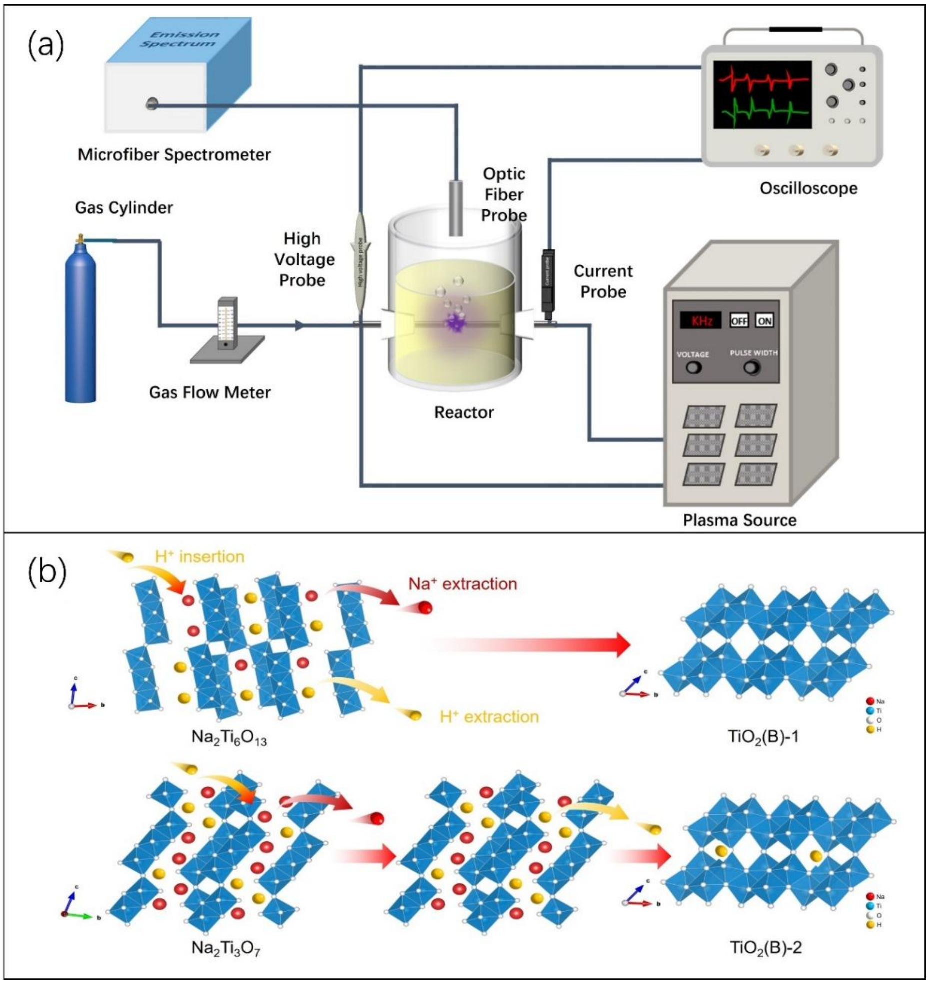

Scheme 1. (a) Schematic illustration of needle-type plasma-catalysis apparatus for the preparation of H_2O_2; (b) Insertion/Extraction mechanism of ions in the crystal structure of sodium titanate and the phase transition process to bronze TiO_2.

2.3 Plasma characterization

The concentration of H ions of solution was measured with a FE28-Standard Mettler pH meter (range: 0.00~14.00 pH, resolution: 0.01 pH, accuracy: ± 0.01 pH). The conductivity of the solution was collected using a LAQUA ES-71G act conductivity meter. Optical emission spectroscopy signal (OES) of liquid phase plasma was captured with a NOVA-EX 400-001-5685 Ocean Optics' fiber optic spectrometer. Electron spin resonance (ESR) signals of 5, 5-dimethyl-1-pyrroline-n-oxide (DMPO) spin-trapped radicals were recorded using a Bruker EMXnano spectrometer at 298 K and 9.63 GHz. Using GWINSTEK GDS-2202A hybrid digital oscilloscope to acquire the values of pulse current and pulse voltage of liquid phase plasma at a high-speed sampling rate of 2 GS/s.

2.4 In-situ FT-IR spectra to distinguish the H_2O_2 adsorption on TiO_2

First, the TiO_2 catalyst was placed in an in-situ infrared diffuse reflectance cell. Under an argon gas flow, the catalyst was heated to 120°C to remove surface-adsorbed impurities. The infrared spectrum collected at this stage served as the background. Subsequently, high-purity Ar was bubbled through a porous gas washing bottle containing 30% H_2O_2, introducing H_2O_2 vapor into the gas-solid infrared diffuse reflectance cell. After flowing the gas for 30 minutes, UV light was turned on to irradiate the surface of TiO_2, and infrared spectra were collected at various illumination times.

3. Results and discussion

Ensuring the efficiency of H_2O_2 generation while minimizing its decomposition is crucial for improving the photocatalysis in high-energy environments, such as plasma field. Due to the high reactivity of H_2O_2, it can readily react with the TiO_2 surface, particularly when the surface is disordered. The preparation of highly crystalline TiO_2, minimizing disorder and surface defects, is key to controlling H_2O_2 decomposition in TiO_2 systems. Among the various phases of TiO_2, bronze is notable for its unique properties. The diffusion coefficient of H_2O_2 on the representative (001) facet of bronze TiO_2 is the highest [30], indicating the lowest degree of H_2O_2 decomposition. Traditional methods for synthesizing bronze TiO_2 involve hydrogen ion exchange and dehydration of $Na_2Ti_nO_{2n+1}$ precursors, typically limited to n=1-3[31, 32]. These methods often result in TiO_2 with defects and impurity phases, which can lead to a phase transition from bronze to anatase, reducing the ability to inhibit H_2O_2 decomposition. In this study, we developed a strategy utilizing an n=6 precursor, $Na_2Ti_6O_{13}$. This precursor has a more ordered structure, better matching the bronze TiO_2 crystal structure [33]. The interlayer tunnels in $Na_2Ti_6O_{13}$ facilitate ion exchange and structural transformation to bronze TiO_2.

3.1 Structural and morphological characterization of bronze TiO_2

We investigated the structural evolution of sodium titanate precursors and their transformation to bronze TiO_2. Figure 1a shows the XRD pattern of the precursor $Na_2Ti_6O_{13}$ prepared by the molten salt method. The diffraction peaks at 2θ = 11.84°, 14.10°, 24.48°, 30.11°, 33.48°, 43.28°, 44.25°, and 48.58° correspond to the (200), (-201), (110), (-203), (402), (602), and (020) planes of monoclinic $Na_2Ti_6O_{13}$ (PDF#73-1398) with lattice constants a = 1.5131 nm, b = 0.3745 nm, and c = 0.9159 nm. In contrast, Figure 1b presents the XRD pattern of the precursor $Na_2Ti_3O_7$, also prepared by the molten salt method. The diffraction peaks at 2θ = 10.52°, 15.84°, 25.68°, 43.88°, and 66.87° correspond to the (100), (101), (110), (104), and (124) planes of monoclinic $Na_2Ti_3O_7$ (PDF#72-0148) with lattice constants a = 0.8571 nm, b = 0.3804 nm, and c = 0.9135 nm. After proton exchange and dehydration, these sodium titanate phases undergo topotactic transformation to bronze TiO_2. In Figure 1c, the diffraction peaks at 2θ = 14.19°, 15.20°, 17.44°, 24.93°, 28.61°, 29.70°, 30.67°, 33.19°, 43.50°, 44.50° and 48.53°correspond to the (001), (200), (20-1), (110), (002), (40-1), (400), (310), (003), (60-1), and (020) of monoclinic bronze TiO_2 (JCPDS 46-1237), respectively. The sharp and narrow peaks indicate that TiO_2(B)-1 has good crystallinity and high purity. In contrast, TiO_2(B)-2 exhibits broad peaks and lacks the characteristic peaks at 2θ = 15.20° and 30.67° corresponding to the (200) and (400) planes of bronze TiO_2. Additionally, the TiO_2(B)-2 shows an unknown diffraction peak at 2θ=12.14°, indicating the presence of impurities. Therefore, XRD characterization indicates that we synthesized and controlled the crystal phase and crystallinity of bronze TiO_2. The $Na_2Ti_6O_{13}$ precursor can be used to synthesize bronze TiO_2 with higher crystallinity and purity.

The difference between the two bronze TiO_2 samples can be attributed to the crystal structures of the precursors, $Na_2Ti_3O_7$ and $Na_2Ti_6O_{13}$. $Na_2Ti_3O_7$ contains three TiO_6 octahedra connected by shared edges to form strip, which in turn share corners to create a serrated $(Ti_3O_7)^{2-}$ layer with an open lamellar structure [34]. In contrast, $Na_2Ti_6O_{13}$ features TiO_6

octahedra sharing edges along the c-axis, forming serrated layers that create larger quasi-rectangular tunneling spaces [35]. As illustrated in Scheme 2, the larger tunneling structure of $Na_2Ti_6O_{13}$ can accommodate more amount of H_2O and H_3O^+, and its stable physical structure can further improve the exchange rate of protons during the hydrothermal reaction. We conducted ICP elemental analysis on the sodium residue in the two bronze TiO_2 samples (Table S1) and found that 98.87% of the sodium in the $Na_2Ti_6O_{13}$ precursor could be exchanged, whereas only 69.76% of the sodium in the $Na_2Ti_3O_7$ precursor could be exchanged. The ICP results further confirm that the residual sodium cations in TiO_2(B)-2 lead to non-homogeneous dehydration reactions and partial distortion of the domain structure, resulting in the low crystallinity of TiO_2(B)-2.

The Raman spectra exhibited sharp and intense peaks, indicating a well-ordered long-range structure and regular lattice arrangement. The Raman signals for $Na_2Ti_6O_{13}$, shown in Figure 1d, match previously reported spectra [36]. A vibration peak at 137 cm^{-1} corresponds to the O-Ti-O bond, while characteristic peaks at 194 and 275 cm^{-1} are associated with the Na-O-Ti bond. Within the range of 400 cm^{-1} to 900 cm^{-1}, various stretching vibration peaks of the TiO_6 octahedron are observed, including a peak at 480 cm^{-1} corresponding to the Ti-O-Ti bond. The peak at 871 cm^{-1} is attributed to the stretching vibration of the short Ti-O bond coordinated with sodium ions and non-bridging oxygen. Figure 1e displays the Raman data for $Na_2Ti_3O_7$, with a vibration peak at 147 cm^{-1} corresponding to the O-Ti-O bond, and characteristic peaks at 192 and 269 cm^{-1} for the Na-O-Ti bond. Similarly, within the 400 cm^{-1} to 900 cm^{-1} range, various stretching vibration peaks of the TiO_6 octahedron are present, including a peak at 401 cm^{-1} for the Ti-O bond and a peak at 835 cm^{-1} for the short Ti-O bond coordinated with sodium ions and non-bridging oxygen [37]. Notably, a Raman signal at 101 cm^{-1} in $Na_2Ti_3O_7$ is absent in $Na_2Ti_6O_{13}$, highlighting structural differences between the two materials.

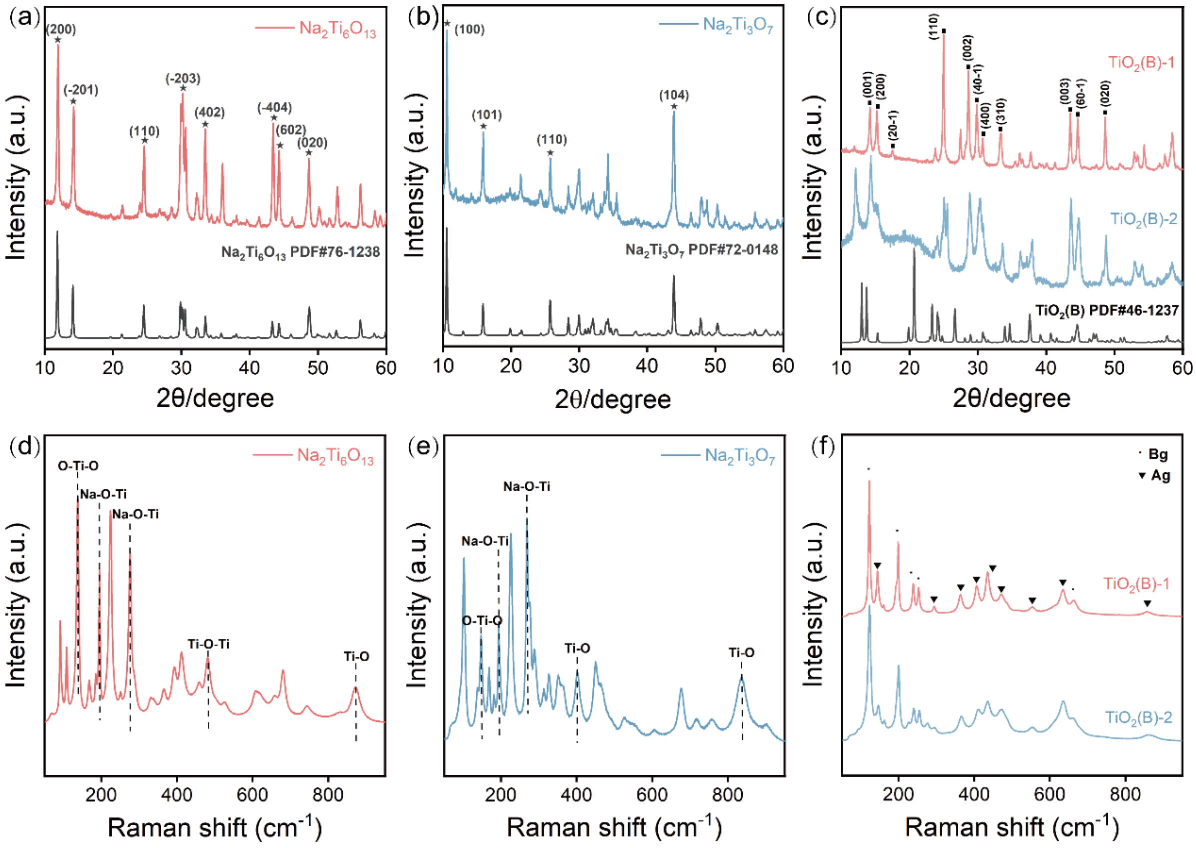

Figure 1. (a-c) XRD patterns of different samples; (b) Raman spectra of different samples.

After proton exchange and dehydration, all Raman bands in Figure 1f of both samples are consistent with the vibrational modes Ag (144, 363.4, 405.4, 435, 472, 554, 634.7 cm^{-1}) and Bg (122, 198.7, 238.5, 253, 663.4

cm^{-1}) of bronze TiO_2 [38]. Compared to TiO_2(B)-1, the Raman peaks of TiO_2(B)-2 are broader and less defined, further confirming the superior crystallinity of the TiO_2(B)-1 material.

We further characterized the morphology and structure of the obtained bronze TiO_2 using SEM, TEM, and HRTEM. Figures 2a-d show SEM images of the prepared bronze TiO_2, revealing a one-dimensional structure the same to that of precursor (Figure S2). Both bronze TiO_2 exhibit a nanobelt morphology, consistent with their precursors. This consistency is attributed to the topotactic transformation from sodium titanate to TiO_2, where the monoclinic phase of sodium titanate favors the formation of monoclinic bronze TiO_2[32]. The diameter of TiO_2(B)-1 nanobelts ranges from 20 to 100 nm, with lengths extending to several micrometers. In contrast, the TiO_2(B)-2 nanobelts have diameters ranging from 50 to 500 nm and lengths up to 30 µm. By comparison, the TiO_2 nanobelts derived from $Na_2Ti_3O_7$ display less uniformity compared to those from $Na_2Ti_6O_{13}$. This discrepancy can be partially explained by the incomplete proton exchange in $Na_2Ti_3O_7$ and the slightly lower lattice match between $Na_2Ti_3O_7$ and bronze TiO_2, leading to uneven internal stress during the topotactic transformation and resulting in less ordered TiO_6 octahedral arrangements. High-resolution TEM results corroborate these observations. As shown in Figure 2e-h, TiO_2(B)-1 exhibits a clearer lattice arrangement with a better-defined shape and smoother surface, indicative of its higher crystallinity. The lattice spacings of 0.64 nm for TiO_2(B)-1 and 0.62 nm for TiO_2(B)-2 correspond to the (0 0 1) crystal plane of bronze TiO_2. The slight differences in observed lattice spacings are likely due to variations in the unit cell parameters of the sodium titanate precursors. The element mapping images of TiO_2(B)-1 in Figure 2i, j confirms uniform distribution of Ti and O along the nanobelts. In Figure 2k, the well aligned spots in SAED pattern of an individual TiO_2 nanobelts proves the highly crystalline nature of the TiO_2(B)-1 nanobelt. In contrast, Figure 2l displays bright spots and a series of faint rings, suggesting that TiO_2(B)-2 is partially crystallized. This crystallinity difference between TiO_2(B)-1 and TiO_2(B)-2 agrees with the XRD and Raman results in Figure 1.

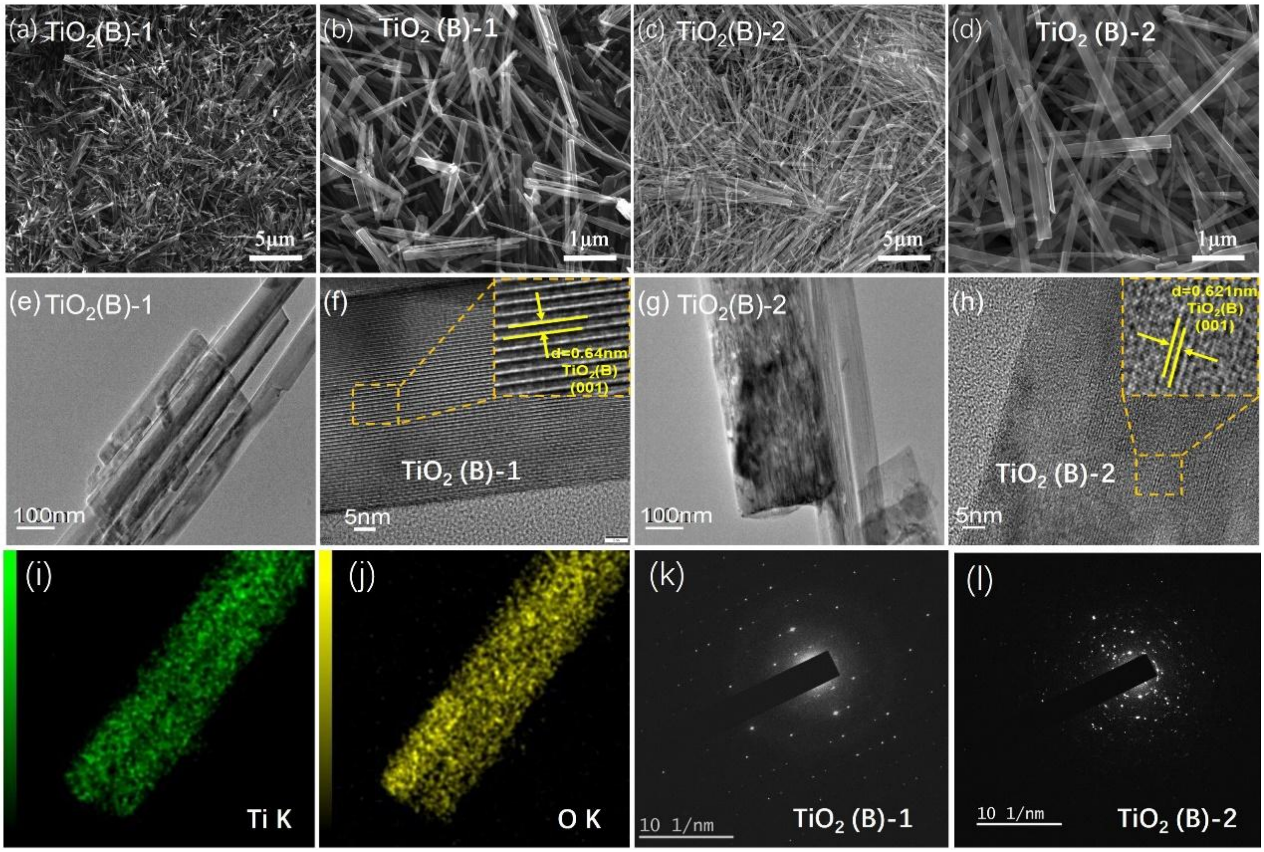

Figure 2. SEM images of different samples: (a, b) TiO_2(B)-1; (c, d) TiO_2(B)-2. TEM and HRTEM images of different samples: (e, f) TiO_2(B)-1; (g, h) TiO_2(B)-2. (i, j) elemental mapping images of TiO_2(B)-1. SAED pattern of (k) TiO_2(B)-1; (l) TiO_2(B)-2.

3.2 H_2O_2 production by a single solution plasma system

We optimized the plasma discharge parameters for H_2O_2 synthesis via solution plasma by varying the gas environment (no gas (Wo), Ar, O_2). As shown in Figure 3a, the presence of gases significantly increased the yield of H_2O_2. Specifically, the total yield increased by 5.42 times with O_2 and 3.21 times with Ar compared to the absence of gas. Additionally, the yield with O_2 was 1.68 times higher than with Ar. Accordingly, O_2 bubbling significantly enhances the production of H_2O_2 through liquid-phase plasma discharge. Figure 3b shows a photo of the discharge spark during the liquid-phase plasma system. In the absence of gas, weak filamentary discharge channels form between the electrodes, resulting in a narrow plasma discharge area. However, the presence of gas significantly expands the plasma area. The discharge channel range is notably enhanced by the rupture of gas bubbles. Water molecules, being highly electronegative, absorb many electrons in the initial discharge stage, making it difficult to form an electron avalanche. Consequently, a large breakdown voltage is required to directly breakdown water and produce plasma. Gas bubbles, however, greatly reduce the breakdown voltage, resulting in a more intense high-energy plasma.

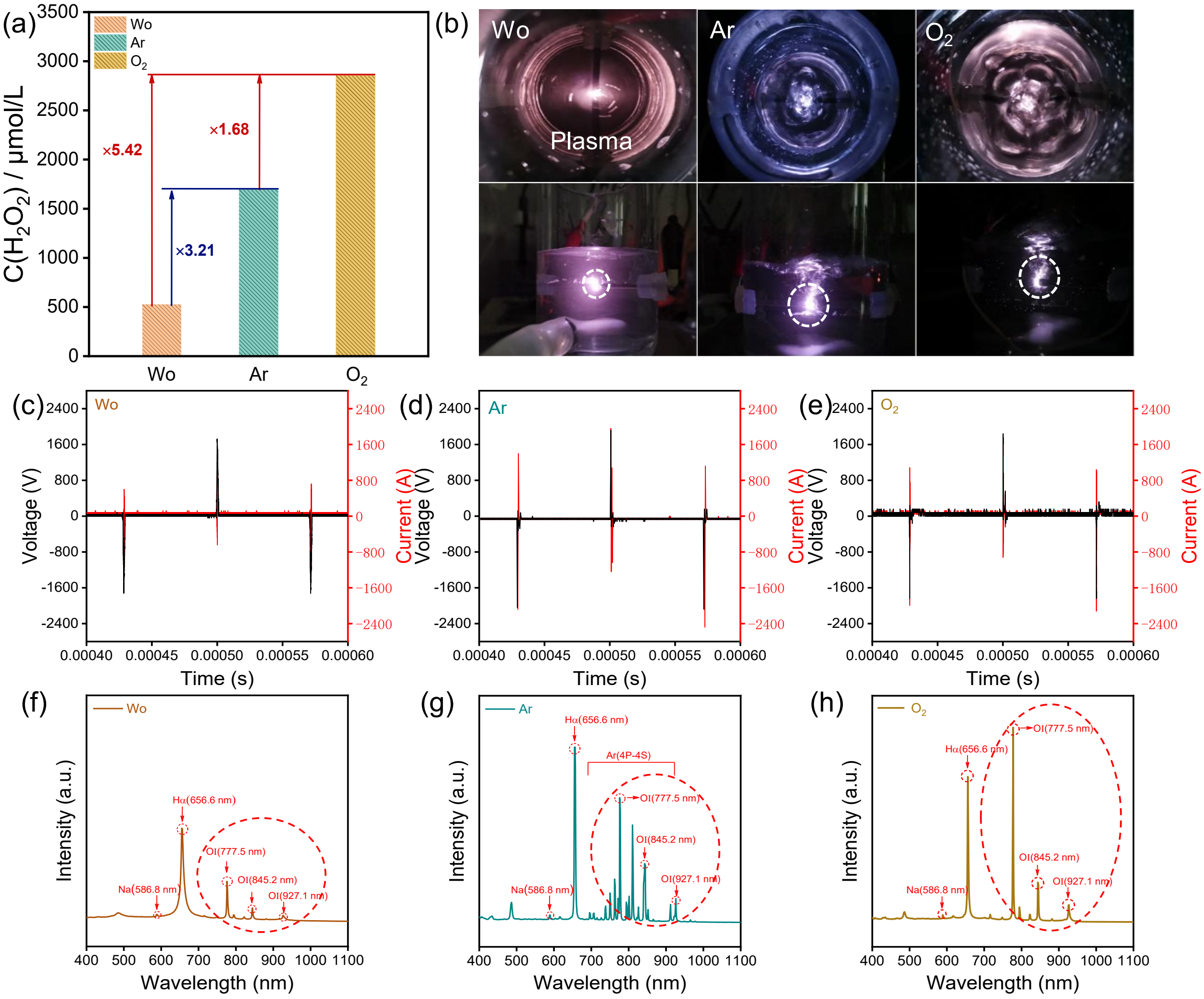

Figure 3. (a) Evaluation of the H_2O_2 yield of liquid-phase plasma at different atmospheres for 1 hour. (b) Schematic illustration of spark in liquid-phase plasma at different atmospheres. (c-e) Voltage and current signals of liquid-phase plasma (Parameters of the pulsed plasma generator: V = ±3 kV, f = 7 kHz, Δt= 3μs) at different atmospheres: (c) without gas; (d) Ar; (e) O_2. (f-h) OES signal of liquid-phase plasma at different atmospheres: (f) without gas; (g) Ar; (h) O_2.

We further characterized and analyzed the effect of the gas on the plasma combining a digital oscilloscope and a fiber optic spectrometer to acquire the pulse current, pulse voltage signal, and emission spectrum of the atoms during the discharge. A 10 Ω resistor was connected in series within the plasma output circuit, and the actual pulse voltage and current generated during the discharge process were monitored using an oscilloscope. As shown in Figure 3c-e, the discharge of the system without gas is unstable, with significant fluctuations in the current value. After introducing gas, both current and voltage values increased, with voltage rising from ±1600 kV to ±2200 kV and current from 800 A to 2000 A. This indicates that the increase in H_2O_2 production after gas injection is partly due to changes in the discharge. The higher peak pulse voltage increases the energy injected into the electrode gap, raising the density of high-energy electrons and thus the frequency of electron collisions with ground-state neutral species, leading to the excitation of more active species and promoting H_2O_2 production.

We diagnosed the active species in the excited state within the plasma by optical emission spectroscopy (OES). To quantitatively compare the intensity of the emission spectra, we normalized the data based on the sodium atomic emission intensity of 100 μL of 10 M NaOH. As shown in Figure 3f, in the absence of gas, the plasma primarily ionizes to excite H_2O molecules, with Hα atomic emission lines at 656.6 nm, O ($3P^5P^0 \rightarrow 3S^53S^0$) at 777.5 nm and 845.2 nm ($3P^3P^0 \rightarrow 3S^3S^0$), and OI atomic emission lines at 927.1 nm [39]. Figure 3g shows that when Ar is added, atomic emission spectra belonging to the 4P-4S orbitals of Ar appear in the range of 700-900 nm, along with increased intensity of the Hα and OI atomic emission spectra [40]. The presence of a large number of metastable Ar species with high excitation energy and long lifetime in the liquid increases the collision frequency of neutral gas molecules with free electrons, further promoting water ionization. As shown in Figure 3h, the most intense emission of oxygen atoms is observed when the system is filled with O_2 compared to Ar, indicating a significant increase in the content of oxygen-active species within the solution. Additionally, the collision reaction of water molecules with excited-state oxygen atoms (O(ID)) can generate ·OH, further promoting the synthesis of H_2O_2.

Besides, we have explored the effects of other gases, such as N_2 and CO_2, on H_2O_2 synthesis during the plasma discharge process. For the case of N_2 atmosphere, discharge in N_2 introduces nitrate and nitrite ions into the solution. The accumulation of these ions increases the solution conductivity, which destabilizes the plasma discharge and makes it unsustainable for H_2O_2 production. For the case of CO_2 atmosphere, similarly, CO_2 discharge leads to the formation of carbonate ions, which also raise the solution conductivity, resulting in unsustainable plasma discharge conditions.

3.3 H_2O_2 production by bronze TiO_2 tuned photocatalysis in solution plasma

We have explored several plasma parameters on the production of H_2O_2, as shown in Figure S3. Increasing the pulse voltage enhances the energy input into the plasma, which promotes water dissociation and radical formation, thereby increasing H_2O_2 yield. However, when voltage is higher than 3 kV, the yield of H_2O_2 is hardly increased. The frequency of the pulse affects the rate at which radicals are generated and recombined, optimizing the conditions for H_2O_2 synthesis. Adjusting the pulse width balances the plasma discharge duration and relaxation period, impacting the stability and accumulation of H_2O_2. Through systematic optimization, we identified 3 kV, 7 kHz and 3 μS as the optimal conditions for maximizing H_2O_2 yield.

We further constructed a bronze TiO_2 mediated plasma-catalytic system to produce H_2O_2 under oxygen bubbling conditions. As shown in Figure 4a, TiO_2 nanobelts can be uniformly dispersed in water to form a slurry, ensuring sufficient contact between the plasma and TiO_2. The introduction of oxygen bubbles further promotes the dispersion of the catalyst and plasma discharge, forming a solid-liquid-gas-plasma four-phase interface that maximizes the reaction efficiency. Evaluation of the H_2O_2 yield is shown in Figure 4b, where all TiO_2 catalysts effectively promoted H_2O_2 synthesis compared to a single plasma system. Among them, the plasma-catalysis system using TiO_2(B)-1 nanobelts had the highest yield, increasing by 352.2 μmol/L (P25), 642.6 μmol/L (TiO_2(B)-2), and 696.8 μmol/L (TiO_2(B)-1), respectively. We found that the high crystallinity TiO_2(B)-1 nanobelts could effectively synergize with the liquid-phase plasma discharge technique to prepare H_2O_2. Remarkably, the maximum H_2O_2 concentration reached 3.5 mmol/L, which is 1-3 orders of magnitude higher than conventional TiO_2 photocatalytic H_2O_2 production methods.

The activity of as-synthesized high crystallinity TiO_2(B)-1 nanobelts outperforms TiO_2(B) nanosheets and nanotube synthesized according to the literature [41, 42], as well as single phase of anatase or rutile TiO_2 (Figure S4). Moreover, the H_2O_2 concentration achieved by gas-phase plasma discharge is lower than that of solution plasma discharge. Even with array

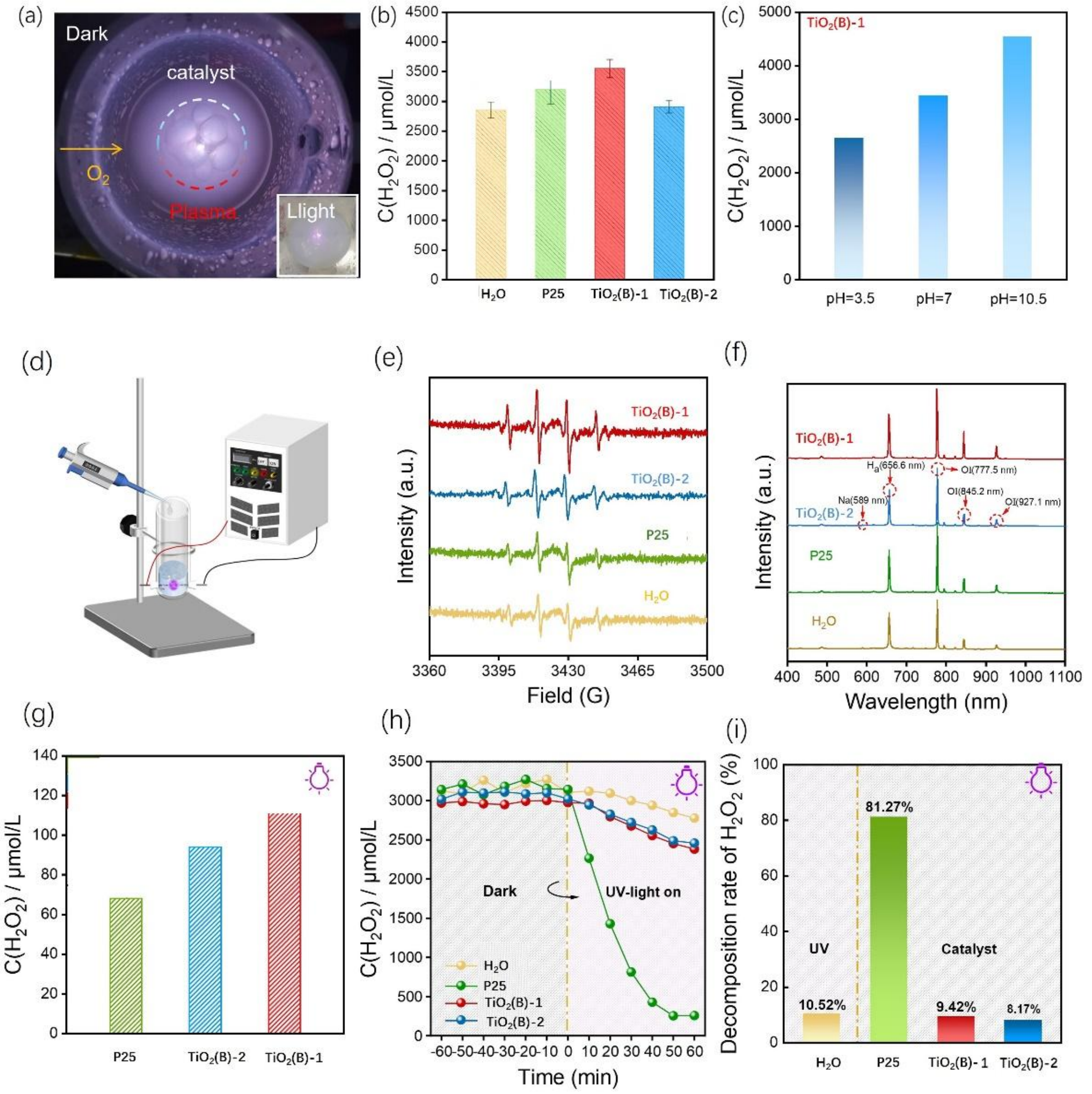

Figure 4. (a) Photo of TiO_2 in solution plasma with gas-liquid-solid-plasma four-phase interfaces; (b) Evaluation of H_2O_2 yield with different catalysts in plasma-catalysis reaction system (Parameters: V = ±3 kV; f = 7 kHz; Δt= 3 μs; O_2 = 1 L/min; (c) pH dependent production of H_2O_2 using $TiO_2(B)$-1; (d) Schematic illustration of the detection of OH· radicals in plasma-catalysis reaction system; (e) detected DMPO- OH· signals by using different TiO_2; (f) detected OES signals by using different TiO_2; (g) photocatalytic production of H_2O_2 by different TiO_2 (Intensity: 55 mW/cm^{-2}; O_2: 1 L/min; 3000μmol/L H_2O_2); (h) Time dependent photocatalytic degradation of H_2O_2 over different TiO_2; (i) Comparison of H_2O_2 decomposition ratio by different TiO_2.

electrodes in gas-phase plasma discharge, the accumulation rate of H_2O_2 only reached 0.95 mM per hour, which is still below the performance of our solution plasma discharge method (Figure S5). We also conducted five long-term stability tests on the TiO_2 (B) system, and all results showed no significant decrease in activity. This indicates that the bronze TiO_2 system exhibits stable H_2O_2 accumulation activity during catalytic processes (Figure S6). These results reveal the efficiency of photocatalyst-mediated solution plasma for H_2O_2 synthesis, demonstrating its potential as a highly effective method for H_2O_2 production.

To analyze the main reaction pathways of the plasma-catalysis system and the effect of solution changes on products, we conducted comparative experiments using $TiO_2(B)$-1 nanobelts at different pH levels. As shown in Figure 4c, alkaline solutions were more favorable for H_2O_2 synthesis. The yield of H_2O_2

at pH = 10.5 is 1.28 times higher than at pH = 7 and 1.7 times higher than at pH = 3.5. Since the alkaline solution provides larger amount of OH^-, we believe that the production of H_2O_2 is partially contributed by OH^- excited species.

We further examined the role of hydroxyl radicals (·OH) in the production of H_2O_2, serving as a crucial indicator for evaluating the production mechanism of H_2O_2. To quantify the ·OH content in the liquid phase, we employed DMPO as a trapping agent. We designed a micro plasma reactor (Figure 4d) to test the instantaneous radical content. Initially, 100 mL of deionized water and 0.020 g of catalyst were uniformly dispersed using an ultrasonic homogenizer. A 2 mL aliquot of the homogenized sample was then placed in the reactor. During discharge, 55 μL of DMPO was added, and the liquid was subsequently placed into a capillary tube to measure the trapped ·OH content. Figure 4e presents the ESR spectra of DMPO-·OH for different samples introduced into the plasma system. In a pure water environment, a characteristic ·OH signal with an intensity ratio of 2:2:1 was detected [43]. The trend in ·OH content across different systems is consistent with the H_2O_2 yield results. The introduction of catalysts enhanced the ·OH signal intensity, with the trend in ·OH content across different systems consistent with the H_2O_2 yield results. Furthermore, the pH-dependent catalytic activity suggests that the higher H_2O_2 yield under alkaline conditions likely originates from the abundant OH^- ions, which combine with high-energy electrons in the plasma to generate a substantial amount of ·OH radical.

Figure 4f illustrates the OES spectra of the plasma-catalysis system. The spectral intensity of the plasma was significantly enhanced after the addition of P25, TiO_2(B)-1 and TiO_2(B)-2 compared to the catalyst-free system. Notably, the plasma-catalysis system using TiO_2(B)-1 nanobelts exhibited the strongest atomic emission intensity (Table S2). The Hα and O atomic emission spectral lines indicated the densities of H and O species, respectively. The enhanced Hα signal peak confirmed that the increased discharge intensity led to greater dissociation of water molecules, while the enhanced OI signal peak indicated that more oxygen atoms were excited and further participated in the synthesis of H_2O_2[44]. This luminescence enhancement is associated with the promotion of plasma discharge by catalyst.

We also monitored the electrical parameters of the plasma generated during the discharge. Figure S7 shows that the voltage increased from approximately ±1900 V to about ±2100 V, and the current increased from 1600 A to 2000 A with the addition of the catalyst. The TiO_2(B)-1 nanobelts induced the largest current and voltage during the solution plasma discharge, which correlated with the strongest luminescence observed. Therefore, bronze-phase TiO_2 enhances plasma discharge, which significantly promotes water dissociation. The primary radical generated during water dissociation is ·OH. While plasma discharge also activates oxygen molecules, our comparative tracking of singlet oxygen and superoxide radicals showed no significant increase in their capture signals. Therefore, we conclude that ·OH are the dominant reactive species, consistent with most reports on plasma-catalytic H_2O_2 synthesis [45].

To evaluate the passive photocatalytic performance of the catalysts in solution plasma, a comparative experiment was conducted. The experimental conditions included a UV light intensity of 55 mW/cm^2, 0.020 g of catalyst, an O_2 flow rate of 1 L/min, and 20 mL of methanol solution as the sacrificial agent. As shown in Figure 4g, the photocatalytic H_2O_2 yields were highest for TiO_2 (B)-1 nanobelts (111.42 μmol/L), followed by TiO_2 (B)-2 nanobelts (94.101 μmol/L), and P25 nanoparticles (68.14 μmol/L). Bronze TiO_2 exhibited superior catalytic effects compared to other crystalline phases, with TiO_2 (B)-1 nanobelts achieving the highest H_2O_2 yield, 1.63 times greater than that of P25 nanoparticles. We compared the light absorption properties of different TiO_2 samples, as shown in Figure S8. We found no consistent correlation between light absorption capacity and catalytic activity. That is, highly crystallized bronze TiO_2 exhibited moderate light absorption intensity-lower than P25 but higher than weakly crystallized bronze TiO_2-yet demonstrated the highest catalytic activity. Thus, we believe that light absorption is only one factor influencing photocatalytic effects, while surface H_2O_2 adsorption capacity and interaction with plasma discharge play more critical roles.

When H_2O_2 does not dissociate immediately from the catalyst surface, electrons migrating to the surface can reduce H_2O_2 to H_2O. Additionally, TiO_2 surfaces form Ti-OOH complexes with H_2O_2, promoting its decomposition under visible light irradiation. To investigate the diffusion behavior of H_2O_2 across different crystalline phases and exposed surfaces, we designed experiments to observe H_2O_2 decomposition under UV light. Figure 4h shows the decomposition effect of H_2O_2 with the catalyst under UV irradiation. Upon UV exposure, H_2O_2 decomposed gradually. In pure water, the decomposition rate was 10.52%, while both TiO_2-based catalysts exhibited slow decomposition rates. Notably, P25 showed the highest

H_2O_2 decomposition ability, achieving an 81.27% decomposition rate under UV light. These differences are attributed to the exposed (001) crystal plane of bronze TiO_2, which facilitates excellent H_2O_2 desorption, leading to a decrease in the decomposition rate. This can be also supported by the results in the literature [30]: On one hand, the diffusion coefficient of H_2O_2 on the surface of bronze-phase TiO_2 is significantly higher than that on anatase-phase TiO_2. This indicates that H_2O_2 desorbs more readily from the bronze-phase TiO_2 surface, which is beneficial for suppressing its decomposition. On the other hand, the adsorption heat of H_2O_2 on bronze-phase TiO_2 (11.3 kJ/mol) is notably lower than that on bronze/anatase TiO_2 heterojunctions (19.4 kJ/mol). A higher adsorption heat corresponds to stronger adsorption of H_2O_2 on the TiO_2 surface. Therefore, the lower adsorption heat of H_2O_2 on bronze-phase TiO_2 compared to anatase-phase TiO_2 suggests weaker adsorption of H_2O_2. Besides, we conducted a radial distribution function analysis of the O-O distance distribution from the AIMD results of H_2O_2 on the TiO_2 surface. The molecular dynamics simulation of H_2O_2-TiO_2(B) and H_2O_2-anatase TiO_2 configuration are depicted in Figure 5a and c. Figure S9 indicates that their kinetic structural relaxations reach a steady state. The simulation results are displayed in Figure 5b. The peak around 1.3 Å corresponds to the O-O bond length in H_2O_2. By analyzing the g(r)-r relationships, we can effectively compare the stability of H_2O_2 molecules on different TiO_2 surfaces. Upon comparison, we observe that the proportion of stable H_2O_2 molecules on the TiO_2(B) surface is significantly higher than that on the anatase phase of TiO_2, which is revealed by a higher value of g(r) for TiO_2(B). This indicates that after kinetic relaxation, TiO_2(B) retains more H_2O_2 on its surface, which is more favorable for stabilizing H_2O_2.

To further investigate the regulation of H_2O_2 synthesis kinetics by the TiO_2 catalyst, we performed a pre-saturation of H_2O_2 adsorption onto the TiO_2 samples. Following this, ultraviolet light was applied, and in-situ infrared spectroscopy was used to track the H_2O_2 adsorption and desorption capabilities of different samples under UV illumination. As shown in Figure S10a, after the TiO_2 (B) sample adsorbed H_2O_2, it exhibited two distinct types of infrared absorption bands. We regarded the bands near 3450 cm^{-1} as a ν(OH) mode of isolated H_2O [46]. Additionally, we observed two weak absorption bands around 3600 and 3700 cm^{-1}, which correspond to the infrared absorption bands of H_2O_2, indicating weak adsorption of H_2O_2 on the TiO_2(B) surface. After UV illumination, the intensity of the H_2O_2 absorption bands rapidly decreased, indicating desorption of H_2O_2 from the TiO_2(B) surface. When the sample was switched to P25

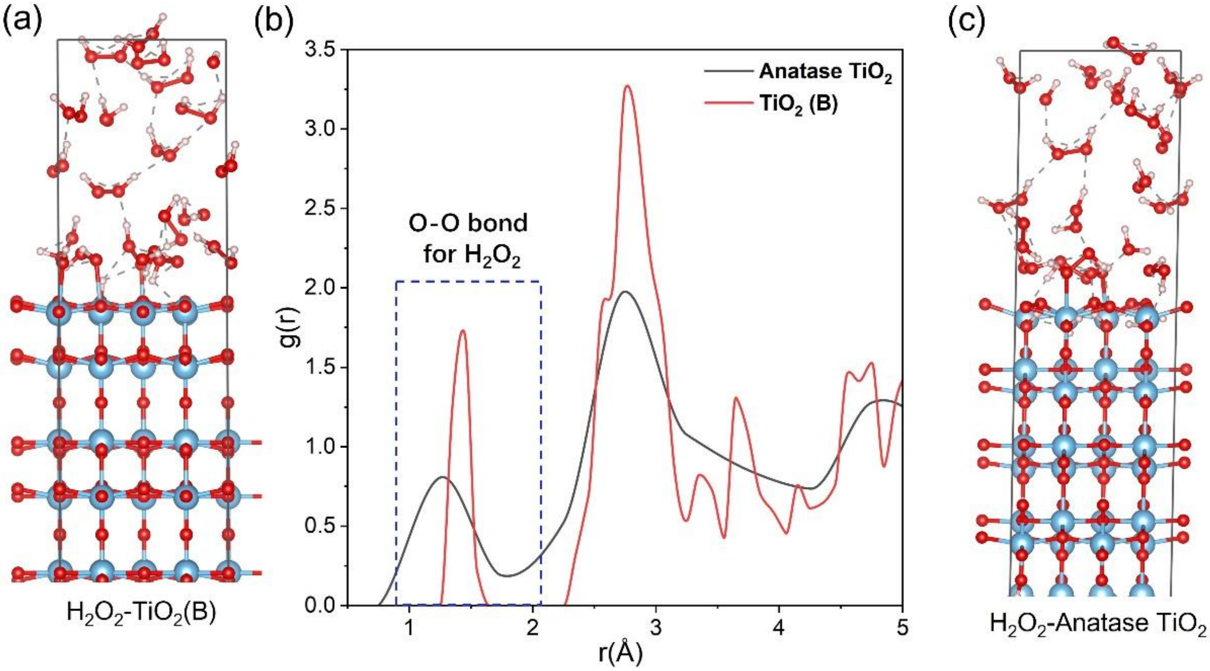

Figure 5. (a) Molecular dynamics simulation of H_2O_2-TiO_2(B) configuration; (b) Radial distribution function of the O-O bond length for H_2O_2-TiO_2 systems; (c) Molecular dynamics simulation of H_2O_2-anatase TiO_2 configuration.

TiO_2, as shown in Figure S10b, we observed two very strong absorption bands at 3600 and 3700 cm^{-1}, which are characteristic absorption bands of H_2O_2 [47]. Notably, these bands did not show significant attenuation after UV illumination, demonstrating strong adsorption of H_2O_2 on P25 TiO_2, with no desorption occurring under UV light. This irreversible adsorption of H_2O_2 on P25 TiO_2 is unfavorable for the accumulation of H_2O_2 in solution. This further confirms our previous observations that P25 TiO_2 readily photocatalyzes the decomposition of H_2O_2, while TiO_2(B) does not facilitate such decomposition.

3.4 Enhanced H_2O_2 production by bronze TiO_2@C in solution plasma

In our study, significant differences were observed in the photocatalytic decomposition of H_2O_2 on the surfaces of bronze and P25 TiO_2. While the bronze surface inhibited H_2O_2 decomposition, the P25 TiO_2 surface did not exhibit this behavior. To further investigate the unique properties of the bronze surface, we coated both materials with carbon. The carbon coating serves to isolate H_2O_2 from direct contact with TiO_2, thereby inhibiting its decomposition. The carbon coating method is depicted in Figure S11. Raman spectroscopy was employed to characterize the carbon-modified TiO_2 (B) samples. Figure S12 shows the Raman spectra of TiO_2 (B)-1@C nanobelts. The spectra revealed two broad peaks corresponding to carbon nanostructures: the D band at 1364 cm^{-1}, indicative of graphite carbon edge vibrations, and the G band at 1585 cm^{-1}, corresponding to the in-plane stretching vibrations of graphite crystals[29]. XRD analysis confirmed that the crystal lattice structure of TiO_2(B) remained unchanged after hydrothermal carbonization. UV-Vis diffuse reflectance spectra showed that TiO_2(B)-1 turned from white to brown after carbonization, exhibiting strong light absorption in the 400-800 nm visible region. XPS spectra also reveals the existence of carbon related peaks on TiO_2 (Figure S13). Combining the XRD, Raman data and XPS, we successfully demonstrated the loading of carbon on the material surface. This result was also validated through surface analysis of carbonized P25 (Figure S14). Figures 6a and b further confirmed the presence of a carbon layer on the TiO_2 surface. After carbon coating, the H_2O_2 content mediated by TiO_2 in solution plasma catalysis increased further (Figures 6c, d). Photocatalytic experiments revealed that the carbon coating further inhibited the decomposition of H_2O_2(Figures 6e, f). Notably, the photocatalytic decomposition of H_2O_2 on the carbon-coated P25 surface was almost equivalent to that on bronze TiO_2, indicating that the carbon coating mitigated the disadvantage of P25 in H_2O_2 decomposition. We compared the pH and conductivity of the liquid-phase discharge system when using TiO_2@C as a catalyst and observed no significant differences (Figure S15). This aligns with the similar H_2O_2 accumulation capabilities of bronze TiO_2 and P25 after carbon loading. Additionally, this indirectly supports the unique characteristics of the brookite TiO_2 surface. These findings demonstrate the importance of surface crystalline composition in the photocatalytic decomposition of H_2O_2 and provide valuable insights for designing TiO_2 or other catalysts suitable for H_2O_2 production in solution plasma environments.

We also analyzed the carbon loading of two samples and found that both had comparable carbon content (ca. 50 atomic%). However, their specific surface areas showed a significant difference, P25 TiO_2 exhibited a specific surface area of 53.5 m^2/g, while TiO_2 (B) had only 28.1 m^2/g. This indicates that although TiO_2 (B) has a smaller surface area, its carbon coating is likely thicker. Such carbon coating not only affects the UV absorption characteristics of TiO_2 but may also partially weaken TiO_2 (B)'s ability to inhibit H_2O_2 decomposition. The carbon coating layer could alter the surface electronic structure or light absorption behavior, further influencing its catalytic performance.

Based on the above results, the production and decomposition trend of H_2O_2 over bronze TiO_2, P25, TiO_2(B)@C and P25@C was illustrated in Figure 7. During plasma discharge in water, hydroxyl radicals are generated. When bronze-phase TiO_2 is introduced into the solution plasma (Figure 7a), the TiO_2 nanobelt structure acts as a medium, enhancing plasma discharge and luminescence, thereby generating more hydroxyl radicals and promoting H_2O_2 formation via hydroxyl radical pathways. Additionally, TiO_2 absorbs UV photons from the plasma channel, preventing the decomposition of the generated H_2O_2. Photogenerated electrons and holes in TiO_2 can react with oxygen bubbles and water molecules, respectively, to produce H_2O_2, thus improving the utilization of plasma energy. Additionally, the decomposition of H_2O_2 is particularly problematic in complex fields, especially under high-energy plasma conditions. Here, bronze-phase TiO_2 not only facilitated the photocatalytic generation of H_2O_2 but also inhibited its decomposition. We improved passive photocatalysis in the solution plasma channel through three routes. Firstly, by adjusting the crystalline phase of TiO_2 (Figure 7a, c), it was found that mixed-phase TiO_2 (anatase/rutile) significantly promoted the photocatalytic decomposition of H_2O_2,

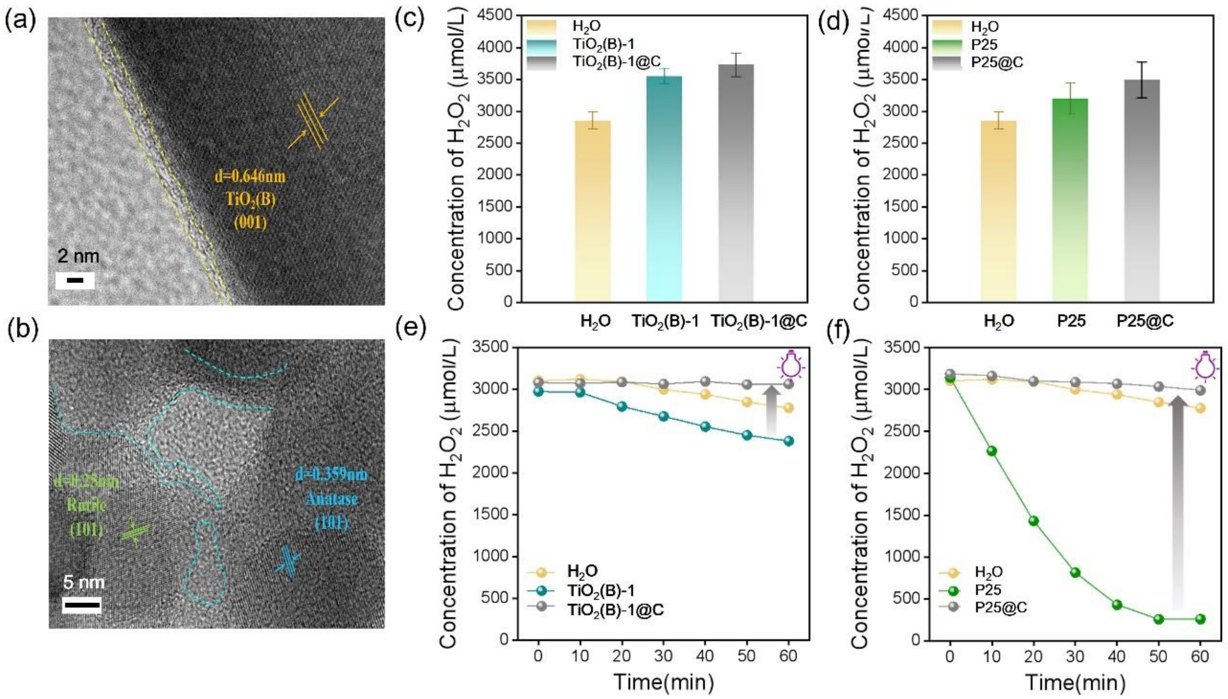

Figure 6. (a) TEM and HRTEM of $TiO_2(B)$@C; (b) TEM and HRTEM of P25@C; (c) Solution plasma production of H_2O_2 mediated by $TiO_2(B)$@C; (d) Solution plasma production of H_2O_2 mediated by P25@C; (e) Comparison on photocatalytic degradation of H_2O_2 at $TiO_2(B)$ and that after carbon coating; (f) Comparison on photocatalytic degradation of H_2O_2 at P25 TiO_2 and that after carbon coating.

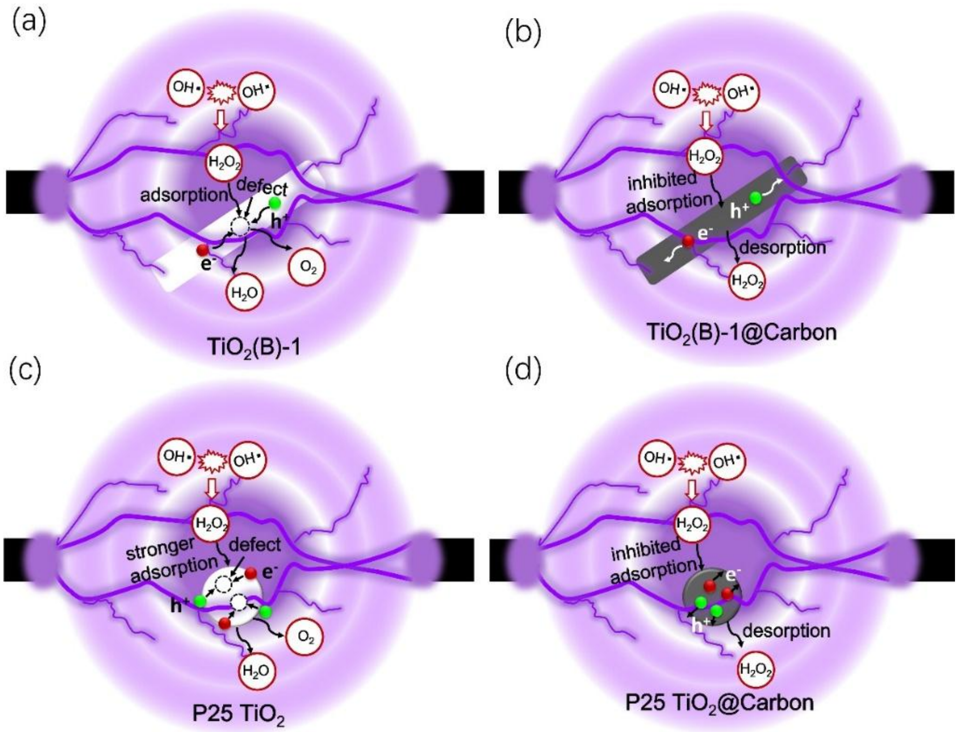

Figure 7. Mechanism diagram for the production of H_2O_2 by plasma-catalysis system with different TiO_2 and TiO_2@carbon.

attributed to the stronger adsorption of H_2O_2 on the anatase surface. In contrast, bronze-phase TiO_2 significantly inhibited the photocatalytic decomposition of H_2O_2. Secondly, by optimizing the crystallinity and purity of the bronze-phase TiO_2, higher-quality growth resulted in enhanced photocatalytic activity, favoring H_2O_2 generation. Thirdly, a uniform carbon layer is coated on the surface of TiO_2 (Figure 7b, d). The carbon coating can further inhibit the adsorption of H_2O_2 on the catalyst surface, which also facilitates the desorption of H_2O_2 from the surface. The moderate strength of adsorption and desorption mediated by the carbon layer promotes the accumulation of H_2O_2 concentration during plasma discharge catalysis.

Last, note that the enhancement of plasma catalytic activity by TiO_2 compared to pure water is not expected several times in other catalytic system, which can be attributed to the inherent constraints of oxide systems. High concentrations of H_2O_2 tend to react with oxide surfaces, forming peroxides and reducing catalytic efficiency. Additionally, the intense energy of plasma is difficult to control, meaning the improvement in catalytic activity is less pronounced than in other catalytic processes, such as electrocatalysis or photocatalysis, which often achieve orders-of-magnitude enhancements [48, 49]. In plasma-catalyst interactions, even a 50% increase in catalytic activity is considered a significant improvement due to the challenges of synergistic effects between plasma and catalysts. Additionally, the plasma catalysis method currently faces challenges such as high energy consumption. However, embracing renewable energy sources and utilizing off-grid options like surplus wind, solar, and electricity can mitigate these issues. Moreover, modular power combinations can facilitate scaling up for industrial production. In terms of H_2O_2 production, plasma catalysis achieves concentrations several orders of magnitude higher than single photocatalysis. While it still lags behind electrocatalysis, plasma catalysis eliminates the need for electrolytes and subsequent separation processes. Therefore, despite current challenges like energy consumption, its advantages-such as eliminating electrolytes and achieving high H_2O_2 concentrations-highlight its potential as a scalable and eco-friendly solution, particularly when integrated with renewable energy systems.

4. Conclusion

In summary, we have developed a clean method for H_2O_2 production using a solution plasma approach. By utilizing the luminescence of the solution plasma field and introducing a suitable photocatalyst, we have achieved enhanced catalytic performance through the synergy of solution plasma and photocatalysis. Bronze-phase TiO_2 nanobelts were prepared using two precursor routes, $Na_2Ti_6O_{13}$ and $Na_2Ti_3O_7$. These nanobelts not only promote plasma discharge but also effectively prevent the photocatalytic decomposition of H_2O_2 on the titanium oxide surface, distinguishing them significantly from traditional TiO_2. The high-crystallinity, high-purity TiO_2 nanobelts prepared via the $Na_2Ti_6O_{13}$ route exhibited superior synergistic catalytic advantages, achieving an H_2O_2 production rate of 3.5 mmol/L/h. This rate is not only the highest concentration value for TiO_2 photocatalytic H_2O_2 production but also exceeds traditional photocatalytic H_2O_2 production rates by 1-3 orders of magnitude. This work provides a valuable reference for studying photocatalysis and synergistic catalysis under complex fields, offering promising avenues for future research in optimizing photocatalytic processes and enhancing catalytic efficiency.

Acknowledgement

This work was supported by Natural Science Foundation of China (Grant Nos. 22572023, 52273236, U22A2078 and 91833303) and the Jilin Province Science and Technology Development Project (Grant Nos. 20220201073GX).

Declaration of Competing Interest

The authors declare that they have no known competing financial interests or personal relationships that could have appeared to influence the work reported in this article. Changhua Wang is an Editorial Board Member of this journal and he was not involved in the editorial review or the decision to publish this article.

References

[1] Chen Ruotian, Ren Zefeng, Liang Yu, Zhang Guanhua, Dittrich Thomas, Liu Runze, Liu Yang, Zhao Yue, Pang Shan, An Hongyu, Ni Chenwei, Zhou Panwang, Han Keli, Fan Fengtao, Li Can. Spatiotemporal imaging of charge transfer in photocatalyst particles. Nature, 2022, 610, 296-301. https://www. nature. com/articles/s41586-022-05183-1

[2] Mateo Diego. Jose Luis Cerrillo, Sara Durinia, Jorge Gascon. Fundamentals and applications of photo-thermal catalysis. Chemical Society Reviews, 2021, 50, 2173-2210. https://doi.org/10.1039/D0CS00357C

[3] Yu Fei, Wang Changhua, Li Yingying, Ma He, Wang Rui, Liu Yichun, Suzuki Norihiro, Terashima Chiaki, Ohtani Bunsho, Ochiai Tsuyoshi, Fujishima Akira, Zhang Xintong. Enhanced solar photothermal catalysis over solution plasma

activated TiO_2. Advanced Science, 2020, 7, 16, 2000204. https://doi.org/10.1002/advs.202000204

[4] Cai Mujin, Li Chaoran, An Xingda, Zhong Biqing, Zhou Yuxuan, Feng Kun, Wang Shenghua, Zhang Chengcheng, Xiao Mengqi, Wu Zhiyi, He Jiari, Wu Chunpeng, Shen Jiahui, Zhu Zhijie, Feng Kai, Zhong Jun, He Le. Supra-photothermal CO_2 methanation over greenhouse-like plasmonic superstructures of ultrasmall cobalt nanoparticles. Advanced Materials, 2024, 36, 9, 2308859. https://doi.org/10.1002/adma.202308859

[5] Zhang Huanjun, Chen Guohua, W Detlef, Bahnemann. Photoelectrocatalytic materials for environmental applications. Journal of Materials Chemistry, 2009, 19, 29, 5089-5121. https://doi.org/10.1039/B821991E

[6] Pan Lun, Sun Shangcong, Chen Ying, Wang Peihong, Wang Jiyu, Zhang Xiangwen, Zou Ji-Jun, Lin Wang Zhong. Advances in piezo-phototronic effect enhanced photocatalysis and photoelectrocatalysis. Advanced Energy Materials, 2020, 10, 15, 2000214. https://doi.org/10.1002/aenm.202000214

[7] Lv Tao, Li Jiaxuan, Arif Nayab, Qi Lu, Lu Jianguo, Ye Zhizhen, Zeng Yu-Jia. Polarization and external-field enhanced photocatalysis. Matter, 2022, 5, 9, 2685-2721. https://doi.org/10.1016/j.matt.2022.06.004

[8] Dharmarathne Leena, Ashokkumar Muthupandian, Grieser Franz. Photocatalytic generation of hydrogen using sonoluminescence and sonochemiluminescence. The Journal of Physical Chemistry C, 2012, 116, 1, 1056-1060. https://doi.org/10.1021/jp209946s

[9] Cheng Tzu-Yang, Chou Feng-Pai, Huang Sheng-Cih, Chang Chin-Yuan, Wu Tung-Kung. Electroluminescence and photocatalytic hydrogen evolution of S, N co-doped graphene oxide quantum dots. Journal of Materials Chemistry A, 2022, 10, 7, 3650-3658. https://doi.org/10.1039/D1TA09917E

[10] Aymen Amine Assadi, Bouzaza Abdelkrim, Vallet Cedric, Wolbert Dominique. Use of DBD plasma, photocatalysis, and combined DBD plasma/photocatalysis in a continuous annular reactor for isovaleraldehyde elimination-Synergetic effect and byproducts identification. Chemical Engineering Journal, 2014, 254, 124-132. https://doi.org/10.1016/j.cej.2014.05.101

[11] Snoeckx Ramses, Bogaerts Annemie. Plasma technology - a novel solution for CO_2 conversion? Chemical Society Reviews, 2017, 46, 19, 5805-5863. https://doi.org/10.1039/C6CS00066E

[12] Xing Yanmei, Wang Changhua, Li Dashuai, Wang Rui, Liang Shuang, Li Yingying, Liu Yichun, Zhang Xintong. Solution plasma processing single-atom Au_1 on CeO_2 nanosheet for low temperature photo-enhanced Mars-van Krevelen CO oxidation. Advanced Functional Materials 2022, 32, 48, 2207694. https://doi.org/10.1002/adfm.202207694

[13] Wang Rui, Che Guangshun, Wang Changhua, Liu Chunyao, Liu Baoshun, Ohtani Bunsho, Liu Yichun, Zhang Xintong. Alcohol plasma processed surface amorphization for photocatalysis. ACS Catalysis, 2022, 12, 19, 12206-12216. https://doi.org/10.1021/acscatal.2c03427

[14] Yi Yanhui, Zhou Juncheng, Guo Hongchen, Zhao Jianli, Su Ji, Wang Li, Wang Xiangsheng, Gong Weimin. Safe direct synthesis of high purity H_2O_2 through a H_2/O_2 plasma reaction. Angewandte Chemie International Edition, 2013, 52, 32, 8446-8449. https://doi.org/10.1002/anie.201304134

[15] Kurake Naoyuki, Tanaka Hiromasa, Ishikawa Kenji, Takeda Keigo, Hashizume Hiroshi, Nakamura Kae, Kajiyama Hiroaki, Kondo Takashi, Kikkawa Fumitaka, Mizuno Masaaki. Effects of •OH and •NO radicals in the aqueous phase on H_2O_2 and NO_2^- generated in plasma-activated medium. Journal of Physics D: Applied Physics, 2017, 50, 15, 155202. https://doi.org/10.1088/1361-6463/aa5f1d

[16] Yan Shiwei, Li Yong, Yang Xinyue, Jia Xiaohua, Xu Jingsan, Song Haojie. Photocatalytic H_2O_2generation reaction with a benchmark rate at air-liquid-solid joint interfaces. Advanced Materials, 2024, 36, 9, 2307967. https://doi.org/10.1002/adma.202307967

[17] Cameli Fabio, Dimitrakellis Panagiotis, Chen Tai-Ying, G Dionisios, Vlachos. Modular plasma microreactor for intensified hydrogen peroxide production. ACS Sustainable Chemistry & Engineering, 2022, 10, 5, 1829-1838. https://doi.org/10.1021/acssuschemeng.1c06973

[18] Chen Qiang, Li Junshuai, Chen Qiang. Kostya (Ken) Ostrikov. Recent advances towards aqueous hydrogen peroxide formation in a direct current plasma-liquid system. High Voltage, 2022, 7, 3, 405-419. https://doi.org/10.1049/hve2.12189

[19] Wu Qi, Wang Changhua, Li Yingying, Zhang Xintong. Enhanced photocatalytic synthesis of H_2O_2 by triplet electron transfer at $g\text{-}C_3N_4@BN$ van der Waals heterojunction interface, Acta Physico-Chimica Sinica, 2025, 41, 9, 100107. https://doi.org/10.1016/j.actphy.2025.100107

[20] He Shanyue, Zhang Xin, Chen Mei, Jiang Hongquan, Qu Yang, Liu Yanduo, Jiang Jizhou. Photocatalytic H_2O_2 production over $Ti(HPO_4)_2$ S-scheme heterojunction through push-pull electronic effects enhance the oxygen reduction. Composite Functional Materials, 2025, 1, 2, 20250203. https://doi.org/10.63823/20250203

[21] Xu Xiang, Zhao Yuying, Yuan Qixin, Wu Yuhan, He Jiawei, Fan Mengmeng. Porous heterostructure of h-BN/carbon as an efficient electrocatalyst for hydrogen peroxide generation. Carbon Letters, 2024, 34, 1629-1637. https://doi.org/10.1007/s42823-024-00718-0

[22] Lukes Petr, Clupek Martin, Babicky Vaclav, Sunka Pavel. Ultraviolet radiation from the pulsed corona discharge in water. Plasma Sources Science and Technology, 2008, 17, 2, 024012. https://doi.org/10.1088/0963-0252/17/2/024012

[23] Huang Yue, Zhang Jinfeng, Ruzimuradov Olim, Mamatkulov Shavkat, Dai Kai, Low Jingxiang. Selective oxygen vacancy engineering for shrinking the potential barrier of S-scheme heterojunction toward highly efficient photocatalytic CO_2 conversion. Composite Functional Materials. 2025, 1, 1,

20250103. https://doi.org/10.63823/20250103

[24] Sun Fanglong, Luo Yadan, Kuang Shaoping, Zhou Min, Ho Wing-Kei, Tang Hua. Ultraviolet-visible-near-infrared light responsive inorganic/organic S-scheme heterojunctions for efficient H_2O_2 production. Journal of Materials Science & Technology, 2025, 229, 287-295. https://doi.org/10.1016/j.jmst.2024.12.060

[25] Yi Yang, Xin Zhou, Miaoli Gu, Bei Cheng, Zhen Wu, Jianjun Zhang. Investigating the charge transfer mechanism of ZnSe QD/COF S-Scheme photocatalyst for H_2O_2 production by using femtosecond transient absorption spectroscopy. Chinese Journal of Catalysis, 2024, 63, 258-269. https://doi.org/10.1016/s1872-2067(24)60069-0

[26] Fu Cong, Liu Lingfang, Li Zhaorui, Wei Yaxiong, Huang Weixin, Zhang Xiaojun. Synergy of bulk defects and surface defects on TiO_2 for highly efficient photocatalytic production of H_2O_2. The Journal of Physical Chemistry Letters, 2023, 14, 34, 7690-7696. https://pubs. acs. org/doi/10. 1021/acs. jpclett. 3c01865

[27] Li Xiangzhong, Chen Chuncheng, Zhao Jincai. Mechanism of photodecomposition of H_2O_2 on TiO_2 surfaces under visible light irradiation. Langmuir, 2001, 17, 13, 4118-4122. https://pubs. acs. org/doi/10. 1021/la010035s

[28] Zou Jian, Gao Jiacheng, Xie Fengyu. An amorphous TiO_2 sol sensitized with H_2O_2 with the enhancement of photocatalytic activity. Journal of Alloys and Compounds, 2010, 497, 1-2, 420-427. https://doi.org/10.1016/j.jallcom.2010.03.093

[29] Wang Liming, Wang Qinggao, Ren Fengzhu, Wang Yuanxu. An unexpected interaction between a H_2O_2 molecule and anatase TiO_2 (101) surface. Applied Surface Science, 2019, 493, 926-932. https://doi.org/10.1016/j.apsusc.2019.07.032

[30] Tu Rui, Chen Shuying, Cao Wei, Zhang Suoying, Li Licheng, Ji Tuo, Zhu Jiahua, Li Jun, Lu Xiaohua. The effect of H_2O_2 desorption on achieving improved selectivity for direct synthesis of H_2O_2 over TiO_2 (B)/anatase supported Pd catalyst. Catalysis Communications. 2017, 89, 69-72. https://doi.org/10.1016/j.catcom.2016.10.024

[31] Shi Yongzheng, Yu Ruomeng, Yang Dongzhi, Liu Yaxin, Qu Jin, Liu Bin, Yu Zhong-Zhen. $Na_2Ti_3O_7$ nanowires with TiO_2 and N-doped carbon dual-shells as binder-free electrodes for efficient sodium storage. Electrochimica Acta, 2019, 321, 134714. https://doi.org/10.1016/j.electacta.2019.134714

[32] Liu B., Boercker J. E., Aydil E. S.. Oriented single crystalline titanium dioxide nanowires. Nanotechnology 2008, 19, 50, 505604. https://doi.org/10.1088/0957-4484/19/50/505604

[33] Seo Dong-Seok, Kim Hwan, Lee Jong-Kook. Hydrothermal synthesis of $Na_2Ti_6O_{13}$ and TiO_2 whiskers. Journal of Crystal Growth, 2005, 275, 1-2, e2371-e2376. https://doi.org/10.1016/j.jcrysgro.2004.11.340

[34] Qamar M., Yoon C. R., Oh H. J., Kim D. H., Jho J. H., Lee K. S., Lee W. J., Lee H. G., Kim S. J.. Effect of post treatments on the structure and thermal stability of titanate nanotubes. Nanotechnology, 2006, 17, 24, 5922-5929. https://doi.org/10.1088/0957-4484/17/24/004

[35] Luo Lan, Zhen Yichao, Lu Yanzhong, Zhou Kaiqiang, Huang Jinxian, Huang Zhigao, Mathur Sanjay, Hong Zhensheng. Structural evolution from layered $Na_2Ti_3O_7$ to $Na_2Ti_6O_{13}$ nanowires enabling a highly reversible anode for Mg-ion batteries. Nanoscale, 2020, 12, 1, 230-238. https://doi.org/10.1039/C9NR08003A

[36] Liu Hongwei, Yang Dongjiang, Zheng Zhanfeng, Ke Xuebin, Waclawik Eric, Zhu Huaiyong, L Ray, Frost. A Raman spectroscopic and TEM study on the structural evolution of $Na_2Ti_3O_7$ during the transition to $Na_2Ti_6O_{13}$. Journal of Raman Spectroscopy, 2010, 41, 10, 1331-1337. https://doi.org/10.1002/jrs.2561

[37] Makal Pronay, Das Debajyoti. Self-doped TiO_2-B single phase, TiO_2-B/anatase and TiO_2-anatase/rutile heterojunctions demonstrating individual superiority in photocatalytic activity under visible and UV light. Applied Surface Science, 2018, 455, 1106-1115. https://doi.org/10.1016/j.apsusc.2018.06.055

[38] Liang Suzhe, Wang Xiaoyan, Qi Ruoxuan, Cheng Ya-Jun, Xia Yonggao, Muller-Buschbaum Peter, Hu Xile. Bronze-phase TiO_2as anode materials in lithium and sodium-ion batteries. Advanced Functional Materials, 2022, 32, 25, 2201675. https://doi.org/10.1002/adfm.202201675

[39] Pongrac Branislav, Simek Milan, Clupek Martin. Vaclav Babicky and Petr Lukes. Spectroscopic characteristics of Hα/OI atomic lines generated by nanosecond pulsed corona-like discharge in deionized water. Journal of Physics D: Applied Physics, 2018, 51, 12, 124001. https://doi.org/10.1088/1361-6463/aaabb1

[40] E A H Timmermans. M J van de Sande, J J A M van der Mullen. Plasma characterization of an atmospheric microwave plasma torch using diode laser absorption studies of the argon 4s 3P2state. Plasma Sources Science and Technology, 2003, 12, 3, 324-334. https://doi.org/10.1088/0963-0252/12/3/305

[41] Xiang Guolei, Li Tianyang, Zhuang Jing, Wang Xun. Large-scale synthesis of metastable TiO_2(B) nanosheets with atomic thickness and their photocatalytic properties, Chemical Communications, 2010, 46, 6801-6803. https://doi.org/10.1039/C0CC02327B

[42] Wang Changhua, Zhang Xintong, Wei Yongan, Kong Lina, Chang Feng, Zheng Han, Wu Liangzhuan, Zhi Jinfang, Liu Yichun. Correlation between band alignment and enhanced photocatalysis: a case study with anatase/TiO_2(B) nanotube heterojunction, Dalton Transactions, 2015, 44, 13331-13339. https://doi.org/10.1039/C5DT01860A

[43] Li Linxiang, Abe Yoshihiro, Kanagawa Kiyotada, Usui Noriko, Imai Kazuhiro, Mashino Tadahiko, Mochizuki Masataka, Miyata Naoki. Distinguishing the 5, 5-dimethyl-1-pyrroline N-oxide (DMPO)-OH radical quenching effect from the hydroxyl radical scavenging effect in the ESR spin-trapping method. Analytica Chimica Act, 2004, 512, 1, 121-124. https://doi.org/10.1016/j.aca.2004.02.020

[44] Li Zheling, Deng Libo, A Ian, Kinloch, J Robert, Young.

Raman spectroscopy of carbon materials and their composites: graphene, nanotubes and fibers. Progress in Materials Science, 2023, 135, 101089. https://doi.org/10.1016/j.pmatsci.2023.101089

[45] Liang Shuang, Wu Qi, Wang Changhua, Wang Rui, Li Dashuai, Xing Yanmei, Jin Dexin, Ma He, Liu Yichun. Sustainable H_2O_2 production via solution plasma catalysis. Proceedings of the National Academy of Sciences, 2024, 121, e2410504121. https://doi.org/10.1073/pnas.2410504121

[46] Allabar Anja, Nowak Marcus. High spatial resolution analysis of H_2O in silicate glass using attenuated total reflection FTIR spectroscopy coupled with a focal plane array detector. Chemical Geology, 2020, 556, 119833. https://doi.org/10.1016/j.chemgeo.2020.119833

[47] Tsuneda Takao, K Raman, Singh, Iiyama Akihiro, Miyatake Kenji. Theoretical investigation of the H_2O_2-induced degradation mechanism of hydrated nafion membrane via ether-linkage dissociation. ACS Omega, 2017, 2, 4053-4064. https://doi.org/10.1021/acsomega.7b00594

[48] Yang Man, Zou Yilun, Ding Lei, Yu Yang, Ma Jinai, Li Lei. Ande Fudja Rafryanto, Jing Zou, Arramel & Haitao Wang. TiO_2 nanoparticles anchored on graphene oxide nanosheets as a highly active photocatalyst for decabromodiphenyl ether degradation. Carbon Letters, 2023, 33, 1333-1341. https://doi.org/10.1007/s42823-022-00456-1

[49] Sayed Mahmoud, Li Han, Bie Chuanbiao. Challenges and prospects of photocatalytic H_2O_2 production. Acta Physico-Chimica Sinica, 41, 9, 2025. https://doi.org/10.1016/j.actphy.2025.100117.